A&A 558, A11 (2013)
DOI: 10.1051/0004-6361/201321934

Astronomy & Astrophysics

Diagnoses to unravel secular hydrodynamical processes in rotating main sequence stars

II. The actions of internal gravity waves

S. Mathis[1], T. Decressin[2], P. Eggenberger[2], and C. Charbonnel[2,3]

[1] Laboratoire AIM Paris-Saclay, CEA/DSM-CNRS-Université Paris Diderot, IRFU/SAp Centre de Saclay, 91191 Gif-sur-Yvette, France
e-mail: stephane.mathis@cea.fr
[2] Geneva Observatory, University of Geneva, chemin des Maillettes 51, 1290 Sauverny, Switzerland
e-mail: [thibaut.decressin;patrick.eggenberger;corinne.charbonnel]@unige.ch
[3] LATT, CNRS UMR 5572, Université de Toulouse, 14 avenue Edouard Belin, 31400 Toulouse Cedex 04, France

Received 21 May 2013 / Accepted 3 July 2013

ABSTRACT

Context. With the progress of observational constraints on stellar rotation and on the angular velocity profile in stars, it is necessary to understand how angular momentum is transported in stellar interiors during their whole evolution. In this context, more highly refined dynamical stellar evolution models have been built that take into account transport mechanisms.
Aims. Internal gravity waves (IGWs) excited by convective regions constitute an efficient transport mechanism over long distances in stellar radiation zones. They are one of the mechanisms that are suspected of being responsible for the quasi-flat rotation profile of the solar radiative region up to 0.2 $R_\odot$. Therefore, we include them in our detailed analysis started in Paper I of the main physical processes responsible for the transport of angular momentum and chemical species in stellar radiation zones. Here, we focus on the complete interaction between differential rotation, meridional circulation, shear-induced turbulence, and IGWs during the main sequence.
Methods. We improved the diagnosis tools designed in Paper I to unravel angular momentum transport and chemical mixing in rotating stars by taking into account IGWs. The star's secular hydrodynamics is treated using projection on axisymmetric spherical harmonics and appropriate horizontal averages that allow the problem to be reduced to one dimension while preserving the non-diffusive character of angular momentum transport by the meridional circulation and IGWs. Wave excitation by convective zones is computed at each time-step of the evolution track. We choose here to analyse the evolution of a 1.1 $M_\odot$, $Z_\odot$ star in which IGWs are known to be efficient.
Results. We quantify the relative importance of the physical mechanisms that sustain meridional currents and that drive the transport of angular momentum, heat, and chemicals when IGWs are taken into account. First, angular momentum extraction, Reynolds stresses caused by IGWs, and viscous stresses sustain a large-scale multi-cellular meridional circulation. This circulation in turn advects entropy, which generates temperature fluctuations and a new rotation profile because of thermal wind.
Conclusions. We have refined our diagnosis of secular transport processes in stellar interiors. We confirm that meridional circulation is sustained by applied torques, internal stresses, and structural readjustments, rather than by thermal imbalance, and we detail the impact of IGWs. These large-scale flows then modify the thermal structure of stars, their internal rotation profile, and their chemical stratification. The tools we developed in Paper I and generalised for the present analysis will be used in the near future to study secular hydrodynamics of rotating stars taking into account IGWs in the whole Hertzsprung-Russell diagram.

Key words. hydrodynamics – waves – turbulence – stars: evolution – stars: rotation

1. Introduction

Understanding the history of the angular momentum of the stars and the way differential rotation develops in their interior during their evolution is one of the key questions of modern stellar physics. In this context, increasing numbers of refined constraints are obtained from observations. First, surface rotation rates have been determined for large stellar samples that give clues on rotational evolution with time along the life of the stars of various types (e.g. Bouvier 2008; Irwin & Bouvier 2009; Meibom et al. 2009; James et al. 2010; Meibom et al. 2011). Next, abundance anomalies observed at stellar surfaces give indirect but powerful constraints on secular mechanisms that transport angular momentum and induce mild mixing of chemicals in stellar radiative zones (e.g. Pinsonneault 1997; Talon & Charbonnel 1998; Maeder 2009, and references therein). Finally, direct constraints are obtained on the rotation profile in solar and stellar interiors, respectively through helioseismology (e.g. García et al. 2007; Mathur et al. 2008b; Eff-Darwich & Korzennik 2012) and asteroseismology (e.g. Aerts et al. 2003; Beck et al. 2012; Deheuvels et al. 2012; Mosser et al. 2012).

Those indirect and direct constraints on the dynamics of stellar interiors in the whole Hertzsprung-Russell diagram strongly motivate the development of new generations of stellar models that consistently take into account transport processes of angular momentum and of chemicals and evaluate their impact on stellar evolution (e.g. Talon et al. 1997; Maeder & Meynet 2000; Palacios et al. 2003; Talon & Charbonnel 2005, 2007; Eggenberger et al. 2008; Maeder 2009). The relevant hydrodydamical (and magneto-hydrodynamical) mechanisms that are believed to act on secular time-scales are i) large-scale meridional circulation driven by external torques and stellar structure adjustments (Zahn 1992; Maeder & Zahn 1998; Mathis & Zahn 2004; Espinosa Lara & Rieutord 2007); ii) turbulence

induced by differential rotation instabilities (Zahn 1983; Talon & Zahn 1997; Maeder 1997, 2003; Mathis et al. 2004; Maeder et al. 2013); iii) internal gravity waves (IGWs), excited by convective regions (Schatzman 1993; Zahn et al. 1997; Kumar et al. 1999; Talon et al. 2002; Talon & Charbonnel 2003, 2004, 2005, 2008; Mathis et al. 2008a; Mathis 2009; Mathis & de Brye 2012); and iv) fossil magnetic fields (e.g. Mestel & Weiss 1987; Rudiger & Kitchatinov 1997; Gough & McIntyre 1998; MacGregor & Charbonneau 1999; Mathis & Zahn 2005; Garaud & Garaud 2008; Spada et al. 2010; Strugarek et al. 2011) and their possible instabilities (Spruit 1999; Eggenberger et al. 2005; Zahn et al. 2007).

It has long been known that Type I rotational transport, i.e. meridional circulation and shear turbulence alone, cannot explain the uniform rotation observed down to 0.2 $R_\odot$ in the solar radiative region (Pinsonneault et al. 1989; Talon & Charbonnel 2005; Turck-Chièze et al. 2010), the new asteroseismic data on internal rotation of subgiant and giant stars (Eggenberger et al. 2012; Ceillier et al. 2012; Marques et al. 2013), or the observed rotation rate of white dwarf stars (Kawaler 1988, 2004; Suijs et al. 2008; Decressin et al. 2009a). These difficulties lead to the conclusion that at least one other process is at work in low-mass stars to transport angular momentum (Talon & Charbonnel 1998). In this context, Charbonnel & Talon (2005) have demonstrated that IGWs, coupled with large-scale meridional circulation and shear-induced turbulence, are able to reproduce the light element abundances at the surface of low-mass stars and to efficiently extract angular momentum from the centre of these stars (see also Talon & Charbonnel 2005, 2004). Additionally, Talon & Charbonnel (2008) showed that IGWs are efficiently excited at various phases of the evolution of both low- and intermediate-mass stars, and may therefore play a key role on the internal dynamics (in particular on the meridional currents and the rotation profile) from the pre-main sequence (Charbonnel et al. 2013) up to the most advanced phases.

In Decressin et al. (2009b, Paper I), we developed a set of diagnoses to unravel the interaction between secular hydrodynamical processes during the main sequence and applied it to models taking into account only meridional circulation and shear turbulence. In the present work, we have chosen to investigate the additional impact of IGWs, while a forthcoming study will be devoted to magnetic field. For this purpose, we present here a generalisation of the relevant diagnoses that will help to visualize the interaction between large-scale meridional flows, turbulence, and IGWs in stellar radiation zones. In Sect. 2, we recall the transport equations for angular momentum, heat, and chemicals taking into account IGWs; we identify processes that sustain meridional circulation and we introduce the diagnosis that will help unravel the highly non-linear interaction between differential rotation, meridional circulation, shear-induced turbulence, and IGWs. In Sect. 3, we describe prescriptions for the studied 1.1 $M_\odot$, $Z_\odot$ stellar model computations. In Sect. 4, we apply our tools to analyse the secular dynamics of the radiation zone of this star during its main-sequence evolution. In Sect. 5, we finally present our conclusions and the perspectives of this work.

2. Formalism

2.1. Main assumptions

As emphasised in Paper I, simulating dynamical processes in stellar interiors in full detail requires including length scales and time scales spanning several orders of magnitude. One can choose either to describe processes such as convection, instabilities, and turbulence that occur on dynamical time scales, or to focus on the long-term evolution, as we do here, where the typical time scale is either the Kelvin-Helmholtz time or that characterizing the dominant nuclear reactions. In this case, considering length scales in the vertical direction, we have chosen the resolution that adequately represents the steepest gradients that develop during the evolution. Concerning the latitudinal direction, one should remember that stellar radiation regions are stably stratified; this leads to an anisotropic turbulent transport, which is stronger in the horizontal direction than in the vertical because of the buoyancy that inhibits turbulent motion in the vertical direction. Therefore, horizontal gradients of all scalar quantities such as temperature and mean molecular weight fluctuations are weak, which allows the projection of secular transport equations in a few spherical harmonics.

Consequently, following Zahn (1992) we assume the rotation to be shellular,

$$\Omega(r,\theta) = \overline{\Omega}(r) = \frac{\int_0^\pi \sin^3\theta\,\Omega\,\mathrm{d}\theta}{\int_0^\pi \sin^3\theta\,\mathrm{d}\theta}. \tag{1}$$

Then, we introduce the macroscopic velocity field, which is split into four components,

$$\boldsymbol{V} = \underbrace{r\sin\theta\,\overline{\Omega}\,\widehat{\boldsymbol{e}}_\varphi}_{1} + \underbrace{\dot{r}\,\widehat{\boldsymbol{e}}_r}_{2} + \underbrace{\boldsymbol{\mathcal{U}}_\mathrm{M}(r,\theta)}_{3} + \underbrace{\boldsymbol{u}}_{4}, \tag{2}$$

with $\widehat{\boldsymbol{e}}_k$, where $k = \{r,\theta,\varphi\}$ are the unit vectors in the radial, latitudinal, and azimuthal directions. Term 1 represents the azimuthal velocity field associated with shellular differential rotation. Term 2 corresponds to the Lagrangian velocity due to the structural readjustments of the star during its evolution. Term 3 is the meridional circulation velocity field that expands only on the $\ell = 2$ spherical function for a shellular rotation

$$\boldsymbol{\mathcal{U}}_\mathrm{M} = U_2(r)\,P_2(\cos\theta)\,\widehat{\boldsymbol{e}}_r + \frac{1}{6\overline{\rho}r}\frac{\mathrm{d}}{\mathrm{d}r}\left[\overline{\rho}r^2U_2\right]\frac{\mathrm{d}P_2(\cos\theta)}{\mathrm{d}\theta}\,\widehat{\boldsymbol{e}}_\theta. \tag{3}$$

The latitudinal component is obtained using the anelastic approximation, i.e. $\boldsymbol{\nabla}\cdot(\overline{\rho}\,\boldsymbol{\mathcal{U}}_\mathrm{M}) = 0$ ($\overline{\rho}$ is the mean density on an isobar, cf. Eq. (7)), where acoustic waves have been filtered out. Moreover, this approximation also allows $\boldsymbol{\mathcal{U}}_\mathrm{M}$ to be expressed as a function of a stream function ($\xi_\mathrm{M}(r,\theta)$) as in Paper I,

$$\boldsymbol{\mathcal{U}}_\mathrm{M} = -\frac{1}{\overline{\rho}}\frac{1}{r\sin\theta}\boldsymbol{\nabla}\xi\times\widehat{\boldsymbol{e}}_\varphi, \tag{4}$$

with

$$\xi_\mathrm{M} = \frac{1}{2}\overline{\rho}r^2U_2\left(\cos^3\theta - \cos\theta\right), \tag{5}$$

where $\boldsymbol{\mathcal{U}}_\mathrm{M}$ is tangent to the iso-ξ line since $\boldsymbol{\mathcal{U}}_\mathrm{M}\cdot\boldsymbol{\nabla}\xi = 0$. This large-scale meridional circulation is driven by external torques such as those associated to stellar winds or tides if there is a companion close to the considered star, and by internal stresses (Zahn 1992; Maeder & Meynet 2000; Rieutord 2006; Decressin et al. 2009b).

We introduce through Term 4 the IGWs velocity field (Zahn et al. 1997)

$$\boldsymbol{u}(r,\theta,\varphi,t) = \sum_{\sigma,\ell,m}\left\{\left[u_{r;\ell}(r)\,Y_\ell^m(\theta,\varphi) + u_{H;\ell}(r)\,\boldsymbol{\nabla}_H Y_\ell^m(\theta,\varphi)\right] \times\exp[-\mathrm{i}\sigma t]\right\} \tag{6}$$

that is expanded in spherical harmonics where ℓ and m are, respectively, the classical orbital and azimuthal numbers. Here, $m > 0$ and $m < 0$ correspond to prograde and retrograde IGWs, respectively and σ is the wave frequency. Finally, we introduce the horizontal gradient $\boldsymbol{\nabla}_H = \partial_\theta \widehat{\boldsymbol{e}}_\theta + 1/\sin\theta\, \partial_\varphi \widehat{\boldsymbol{e}}_\varphi$.

Moreover, each scalar field (X) is written as

$$X(r,\theta) = \overline{X}(r) + \delta X(r,\theta), \quad \text{where} \quad \delta X = \widehat{X}_2(r) P_2(\cos\theta) \quad (7)$$

with its horizontal average on an isobar ($\overline{X}$) and its associated fluctuation δX that is expanded in the $\ell = 2$ spherical function because of the choice of a shellular rotation. In particular, we expand the temperature

$$T(r,\theta) = \overline{T}(r) + \delta T(r,\theta) \quad \text{with} \quad \delta T = \left[\Psi_2(r)\,\overline{T}\right] P_2(\cos\theta) \quad (8)$$

and the mean molecular weight

$$\mu(r,\theta) = \overline{\mu}(r) + \delta\mu(r,\theta) \quad \text{with} \quad \delta\mu = \left[\Lambda_2(r)\,\overline{\mu}\right] P_2(\cos\theta) \quad (9)$$

with Ψ_2 and Λ_2 their relative fluctuations on the isobar.

Finally, the unresolved scales that mostly correspond to the turbulent transport, are described by prescriptions coming from laboratory experiments or numerical simulations and if not from phenomenological considerations (see Sect. 2.6).

2.2. Internal gravity waves

2.2.1. Transport of angular momentum by internal gravity waves

Internal gravity waves are excited both by convective penetration in stable regions (Garcia Lopez & Spruit 1991; Kiraga et al. 2003, 2005; Browning et al. 2004; Dintrans et al. 2005; Rogers & Glatzmaier 2005, 2006; Brun et al. 2011) and in the bulk of convective regions by Reynolds stresses and buoyancy (Goldreich & Kumar 1990; Kumar & Quataert 1997; Belkacem et al. 2009; Samadi et al. 2010, see Sect. 2.2.2). They transport angular momentum and deposit it in the radiative layers at the depth where they are damped in a corotation resonance (Goldreich & Nicholson 1989; Zahn et al. 1997). This modifies the angular velocity of the stars, their internal differential rotation, and their evolution because of the induced modification of internal mixing (Talon et al. 2002; Talon & Charbonnel 2003, 2004, 2005).

Here, we summarize the formalism based on Zahn et al. (1997) that was initially implemented in the stellar evolution code STAREVOL by Talon & Charbonnel (2005). First, we recall that the local momentum luminosity is related to the flux of angular momentum transported by Reynolds stresses caused by IGWs (F_J)

$$\mathcal{L}_J(r) = r^2 F_J(r), \quad \text{where} \quad F_J = \left\langle \overline{\rho} r \sin\theta u_r u_\varphi \right\rangle_{\theta,\varphi} \quad (10)$$

with $\langle\cdots\rangle_{\theta,\varphi} = \frac{1}{4\pi}\int_0^\pi \int_0^{2\pi} -\sin\theta \mathrm{d}\theta\mathrm{d}\varphi$. Assuming both the Jeffreys-Wentzel-Kramers-Brillouin and the quasi-linear assumptions for IGWs (see the detailed discussion in Rogers et al. 2008; Mathis 2009), we write

$$\mathcal{L}_J(r) = \sum_{\sigma,\ell,m} \mathcal{L}_{J;\ell,m}(r_c,\sigma) \exp\left[-\tau_l(r,\widehat{\sigma})\right], \quad (11)$$

where r_c is the radial position of the border of the convective zone that excites IGWs and τ_ℓ is the local damping rate that takes into account the mean molecular weight stratification

$$\tau_\ell = \left[\ell(\ell+1)\right]^{\frac{3}{2}} \int_r^{r_c} K \frac{N N_T^2}{\widehat{\sigma}^4} \left(\frac{N^2}{N^2 - \widehat{\sigma}^2}\right)^{\frac{1}{2}} \frac{\mathrm{d}r'}{r'^3}; \quad (12)$$

K is the thermal diffusivity, while $N^2 = N_T^2 + N_\mu^2$ is the total Brunt-Väisälä frequency; N_T is the buoyancy frequency linked to the entropy stratification given by $N_T^2 = (\overline{g}\delta/H_P)(\nabla_{ad} - \nabla)$ with the usual notations for the temperature gradient $\nabla = \partial \ln \overline{T}/\partial \ln \overline{P}$ and pressure height scale $H_P = |\mathrm{d}r/\mathrm{dln}\,\overline{P}|$; $\overline{g}$ is the horizontal average of the effective gravity $\boldsymbol{g} = \boldsymbol{\nabla}\Phi + \frac{1}{2}\overline{\Omega}^2 \boldsymbol{\nabla}(r\sin\theta)^2$ (Φ is the gravitational potential); and $\delta = -\left(\partial \ln \overline{\rho}/\partial \ln \overline{T}\right)_{P,\mu}$ is introduced by the used generalised equation of state (see Kippenhahn & Weigert 1990, for more details). Similarly, N_μ is the buoyancy frequency related to the chemical stratification given by $N_\mu^2 = (\overline{g}\phi/H_P)\nabla_\mu$, where $\nabla_\mu = \partial \ln \overline{\mu}/\partial \ln \overline{P}$ and $\phi = (\partial \ln \overline{\rho}/\partial \ln \overline{\mu})_{P,T}$. Finally, $\widehat{\sigma}$ is the local Doppler-shifted frequency

$$\widehat{\sigma}(r) = \sigma - m\left(\overline{\Omega} - \Omega_{CZ}\right), \quad (13)$$

where σ is the excitation frequency in the reference frame of the convection zone generating IGWs and Ω_{CZ} corresponds to uniform rotation in the convection zone.

2.2.2. Volumetric generation of internal gravity waves by convective Reynolds stresses and buoyancy

In the present work, we follow Talon & Charbonnel (2005) for the prescription for IGW excitation and adopt the formalism of Goldreich et al. (1994) for acoustic waves adapted by Kumar & Quataert (1997) to describe volumetric stochastic excitation by turbulent convection (we do not consider the possible effects of penetration by plumes, see Sect. 3.3). The momentum luminosity at the convective border is

$$\mathcal{L}_{J;\ell,m}(r_c,\sigma) = r_c^2 F_{J;\ell,m}(r_c,\sigma) = \frac{m}{\sigma} F_{E;\ell}(r_c,\sigma), \quad (14)$$

where $F_{E;\ell}$ is the energy flux per unity frequency

$$F_{E;\ell}(r_c,\sigma) = \frac{1}{4\pi}\int_{r_c}^{R} \left\{ \frac{\overline{\rho}^2}{r^2}\left[\left(\frac{\mathrm{d}\,u_{r;\ell}}{\mathrm{d}r}\right)^2 + \ell(\ell+1)\left(\frac{\mathrm{d}\,u_{H;\ell}}{\mathrm{d}r}\right)^2\right] \times \frac{V^3 L^4}{1+(\omega\tau_L)^{15/2}} \exp\left[-\ell(\ell+1)\frac{h_{\sigma^2}}{2r^2}\right] \mathrm{d}r \right\} \quad (15)$$

and V is the convective velocity, L the radial size of an energy bearing turbulent eddy, $\tau_L \approx L/V$ the characteristic convective time, and $h_\sigma = L\min\left[1,(2\sigma\tau_L)^{-3/2}\right]$ the radial size of the largest eddy at depth r with characteristic frequency σ or greater deduced from the mixing-length theory. The excitation is computed at each evolution time-step and is therefore always fully consistent with the stellar structure.

The damping of each wave in the radiative zone is computed and then summed-up to obtain the total local momentum luminosity as in Eq. (11).

2.3. Transport of angular momentum and meridional circulation

We recall the equation for the evolution of the mean angular momentum when averaging the azimuthal projection of the momentum equation over an isobar and including IGWs (see e.g. Talon & Charbonnel 2005),

$$\overline{\rho}\frac{\mathrm{d}}{\mathrm{d}t}\left(r^2\overline{\Omega}\right) = \underbrace{\frac{1}{5r^2}\partial_r\left(\overline{\rho}r^4\overline{\Omega}U_2\right)}_{1} + \underbrace{\frac{1}{r^2}\partial_r\left(\overline{\rho}\nu_V r^4 \partial_r\overline{\Omega}\right)}_{2} \underbrace{-\frac{3}{8\pi}\frac{1}{r^2}\partial_r\mathcal{L}_J(r)}_{3}. \quad (16)$$

Term 1 represents the transport of angular momentum by meridional circulation, which advective character is conserved. Term 2 is associated with the action of shear-induced turbulence that is modelled as a diffusive process (see Sect. 2.6), where ν_V is the corresponding turbulent viscosity in the vertical direction given in Eq. (37). Term 3 corresponds to the deposit/extraction of angular momentum by IGWs described by Eq. (11). Finally, the Lagrangian operator $\mathrm{d}/\mathrm{d}t = \partial_t + \dot{r}\partial_r$ accounts for contraction and dilatation of the star during its evolution (with the radial velocity $\dot{r}\widehat{\boldsymbol{e}_r}$).

Equation (16) relates meridional circulation to the overall transport of angular momentum. In the asymptotic regime, the left-hand side term is zero and the transport of angular momentum by meridional circulation is exactly balanced by that through shear turbulence and IGWs. In the limit of vanishing turbulent viscosity and transport by IGWs, the rotation profile would adjust so that no meridional currents appear (Busse 1982). In reality, because of the extraction of angular momentum by magnetised wind (see below), and/or its redistribution by structural changes, the left-hand side term is non zero.

Then, following the method given in Paper I, and integrating Eq. (16) over an isobar, we get an equation for the fluxes of angular momentum as carried by the various involved processes,

$$\Gamma(m) = -F_{\rm tot}(r) = -F_{\rm MC}(r) - F_{\rm S}(r) - F_{\rm J}(r), \tag{17}$$

where

$$F_{\rm MC}(r) = -\frac{1}{5}\overline{\rho} r^4 \overline{\Omega} U_2 \tag{18}$$

is the flux advected by the meridional circulation,

$$F_{\rm S}(r) = -\overline{\rho} r^4 \nu_V \partial_r \overline{\Omega} \tag{19}$$

is that associated to the shear-induced turbulence, and

$$F_{\rm J}(r) = \frac{3}{8\pi}\mathcal{L}_{\rm J} \tag{20}$$

is the one deposited/extracted by IGWs. The term $\Gamma(m)$ represents the loss or gain of angular momentum inside the isobar enclosing the mass $m(r)$ (see Appendix A)

$$\Gamma(m) = \frac{1}{4\pi}\frac{\mathrm{d}}{\mathrm{d}t}\left[\int_0^{M(r)} r'^2 \overline{\Omega}\,\mathrm{d}m'\right]. \tag{21}$$

Then, using Eq. (17), we can extract the radial function of the vertical component of the meridional circulation velocity

$$\begin{aligned} U_2 &= \frac{5}{\overline{\rho} r^4 \overline{\Omega}}\left[\Gamma_M(r) - \overline{\rho}\nu_V r^4 \partial_r \overline{\Omega} + \frac{3}{8\pi}\mathcal{L}_{\rm J}\right] \\ &= U_\Gamma + U_V + U_{\mathcal{L}_{\rm J}}. \end{aligned} \tag{22}$$

Finally, we note that we have the following boundary conditions at the top of radiative cores (RC) of low-mass stars ($r = r_t^{\rm RC}$),

$$\frac{\mathrm{d}}{\mathrm{d}t}\left[\int_{r_t^{\rm RC}}^{R} r'^4\,\overline{\rho}\,\overline{\Omega}\,\mathrm{d}r'\right] = -\frac{1}{5} r^4\,\overline{\rho}\,\overline{\Omega}\,U_2 - \mathcal{F}_{\rm ext} + \frac{3}{8\pi}\mathcal{L}_{\rm J}\left(r_t^{\rm RC}\right), \tag{23}$$

where $\mathcal{F}_{\rm ext}$ is the flux of angular momentum carried by magnetic pressure-driven stellar winds (Kawaler 1988; Pinto et al. 2011; Matt et al. 2012) and by tides if there is a close companion (Zahn 1977; Ogilvie & Lin 2007; Remus et al. 2012; Lai 2012) [1].

[1] We also note that for massive stars, we will have at the top of radiative envelopes (RE) ($r = r_{\rm t}^{\rm RE}$)

$$0 = -\frac{1}{5} r^4\,\overline{\rho}\,\overline{\Omega}\,U_2 - \mathcal{F}_{\rm ext}, \tag{24}$$

where $\mathcal{F}_{\rm ext}$ is the flux of angular momentum carried by radiative stellar winds (Ud-Doula et al. 2009; Meynet et al. 2011) and tides and at the top of a convective core (CC) ($r = r_{\rm t}^{\rm CC}$)

$$\frac{\mathrm{d}}{\mathrm{d}t}\left[\int_0^{r_{\rm t}^{\rm CC}} r'^4\,\overline{\rho}\,\overline{\Omega}\,\mathrm{d}r'\right] = \frac{1}{5} r^4\,\overline{\rho}\,\overline{\Omega}\,U_2 - \frac{3}{8\pi}\mathcal{L}_{\rm J}\left(r_{\rm t}^{\rm CC}\right). \tag{25}$$

2.4. Thermal relaxation

Meridional circulation advects the mean entropy ($\overline{S}$) and the temperature field relaxes on the new thermal state. The induced temperature fluctuation $\delta T = \widehat{T}_2(r) P_2(\cos\theta)$ evolution is ruled by the relaxation equation (Mathis & Zahn 2004)

$$\begin{aligned} &\underbrace{\overline{\rho} C_p \frac{\mathrm{d}}{\mathrm{d}t}\widehat{T}_2}_{\overline{\rho}\overline{T}\partial_t\widetilde{S}} - \underbrace{\left[\overline{\rho}\frac{L}{M}\left(\mathcal{T}_{2,\rm Th} + \mathcal{T}_{2,\mathcal{B}}\right)\right]}_{\boldsymbol{\nabla}\cdot(\chi\boldsymbol{\nabla}T) - \boldsymbol{\nabla}\cdot\boldsymbol{F}_H} = \\ &\underbrace{-\overline{\rho}\overline{T} C_p \frac{N_T^2}{\overline{g}} U_2}_{\overline{\rho}\overline{T}U_r\partial_r\overline{S}} + \underbrace{\overline{\rho}\frac{L}{M}\mathcal{T}_{2,\rm N-G}}_{\rho\varepsilon}. \end{aligned} \tag{26}$$

This is an advection/diffusion equation, where the advective term associated with meridional circulation caused by the transport of angular momentum plays the role of a source or sink of heat. The terms $\mathcal{T}_{2,\rm Th}$ and $\mathcal{T}_{2,\mathcal{B}}$ describe the usual spherical diffusion of heat and the component of the divergence of the radiative flux due to the flattening of the isobar by the centrifugal acceleration; $\boldsymbol{\nabla}\cdot\boldsymbol{F}_H$ is the entropy flux carried by the horizontal turbulence. Finally, $\mathcal{T}_{2,\rm N-G}$ corresponds to the coupling with the nuclear energy generation. Their derivation may be found in Paper I and are recalled in Appendix A.

Equation (26) is finally written in the following form, which will be used in Sect. 3.5.

$$\tilde{\mathcal{T}}_{\rm N-S} = \tilde{\mathcal{T}}_{\rm Adv} + \tilde{\mathcal{T}}_{\mathcal{B}} + \tilde{\mathcal{T}}_{\rm Th} + \tilde{\mathcal{T}}_{\rm N-G}, \tag{27}$$

where

$$\tilde{\mathcal{T}}_{\rm NS} = \overline{\rho}\overline{T} C_p \frac{\mathrm{d}\Psi_2}{\mathrm{d}t}, \tag{28}$$

$$\tilde{\mathcal{T}}_{\rm Adv} = -\overline{\rho}\overline{T} C_p \frac{N_T^2}{\overline{g}\delta} U_2, \tag{29}$$

$$\tilde{\mathcal{T}}_{\mathcal{B}} = \overline{\rho}\frac{L}{M}\mathcal{T}_{2,\mathcal{B}}, \tag{30}$$

$$\tilde{\mathcal{T}}_{\rm Th} = \overline{\rho}\frac{L}{M}\mathcal{T}_{2,\rm Th}, \text{ and} \tag{31}$$

$$\tilde{\mathcal{T}}_{\rm N-G} = \overline{\rho}\frac{L}{M}\mathcal{T}_{2,\rm N-G}. \tag{32}$$

2.4.1. The thermal wind equation

Next, once the temperature has relaxed, the new differential rotation profile is obtained through the thermal wind equation

$$\partial_r \overline{\Omega} = -\frac{3\overline{g}}{r^2}\frac{1}{2\overline{\Omega}}\left(\delta\frac{\widehat{T}_2}{\overline{T}} - \varphi\frac{\widehat{\mu}_2}{\overline{\mu}}\right). \tag{33}$$

A new eddy-viscosity (ν_V) is thus obtained because of the modification of the vertical gradient of angular velocity. To close the loop, the meridional circulation is substained if there are some external torques, structural adjustments, and internal stresses. If this is not the case, the circulation vanishes after an Eddington-Sweet time $t_{\rm ES} = \left[\frac{LR}{GM^2}\left(\frac{\Omega_{\rm s}^2 R^3}{GM}\right)\right]^{-1}$ (Busse 1982; Rieutord 2006; Decressin et al. 2009b).

2.5. Transport of nuclides

We recall that the expansion of the transport equation for the nuclides on an isobar leads to an equation for the evolution of the mass fraction of each considered chemical (see also e.g. Meynet & Maeder 2000)

$$\left(\frac{\mathrm{d}X_i}{\mathrm{d}t}\right)_{M_r} = \frac{\partial}{\partial M_r}\left[(4\pi r^2\rho)^2\,(D_\mathrm{V}+D_\mathrm{eff})\,\frac{\partial X_i}{\partial M_r}\right] + \left(\frac{\mathrm{d}X_i}{\mathrm{d}t}\right)_\mathrm{nucl}, \quad (34)$$

where $\mathrm{d}M_r = 4\pi\overline{\rho}r^2\mathrm{d}r$ and D_V is the vertical component of the turbulent diffusivity (see Eq. (37) below). The strong horizontal turbulence leads to the erosion of the advective transport that can then be described as a diffusive process (Chaboyer & Zahn 1992) with the effective diffusion coefficient

$$D_\mathrm{eff} = \frac{(rU_2)^2}{30D_\mathrm{H}}, \quad (35)$$

where D_H is the horizontal component of the turbulent diffusivity (see Eq. (38)). The second term on the right-hand side of Eq. (34) corresponds to the temporal mass fraction evolution of the ith nuclide due to nuclear burning. In the present study we do not account for atomic diffusion.

Equation (34) is complemented by an equation for the time evolution of the relative fluctuation of the mean molecular weight, expressed here in terms of Λ_2:

$$\frac{\mathrm{d}\Lambda_2}{\mathrm{d}t} - \frac{\mathrm{d}\ln\overline{\mu}}{\mathrm{d}t}\Lambda_2 = \frac{N_\mu^2}{\overline{g}\varphi}U_2 - \frac{6}{r^2}D_\mathrm{H}\Lambda_2. \quad (36)$$

We stress that the advective character of the transport of angular momentum by the meridional circulation and its deposit/extraction by IGWs makes the interpretation of the whole hydrodynamics more complex than when the diffusive approximation is used (e.g. Pinsonneault et al. 1989; Heger et al. 2000). This is one of the reasons that pushed us to develop the tools that we describe in Paper I and that we generalise in Sect. 3 to depict the action of IGWs.

2.6. Turbulence and diffusion

The details of turbulence modelling have already been extensively discussed in previous papers, and we recall here the expressions we have chosen following again Talon & Charbonnel (2005).

First, for the vertical turbulent diffusion coefficients ($D_\mathrm{V} \simeq \nu_\mathrm{V}$) we use the expression by Talon & Zahn (1997),

$$D_\mathrm{V} = \frac{Ri_\mathrm{c}}{N_T^2/(K+D_\mathrm{H}) + N_\mu^2/D_\mathrm{H}}\left(r\partial_r\overline{\Omega}\right)^2, \quad (37)$$

where $Ri_\mathrm{c} = 1/6$ is the adopted value for the critical Richardson number. This prescription is now supported by direct numerical simulations of shear-induced turbulence (Prat & Lignières 2013).

Next, for the horizontal turbulent viscosity we use the prescription derived by Zahn (1992),

$$\nu_\mathrm{H} = \frac{r}{C_\mathrm{H}}\sqrt{|2V_2-\alpha U_2|^2+U_2^2}, \quad (38)$$

where C_H is a parameter of order unity, and V_2 is given by Eq. (3). For the vertical turbulent diffusion coefficient, we assume that $D_\mathrm{H} \simeq \nu_\mathrm{H}$.

3. Prescriptions for the 1.1 $M_\odot$ $Z_\odot$ stellar model computations

3.1. Basic input physics

In the following, we apply the formalism described in Sect. 2 to the main-sequence evolution of a rotating star with an initial mass of 1.1 $M_\odot$ at solar metallicity. The model was computed with the implicit Lagrangian stellar evolution code STAREVOL V3.10, with the same basic input physics as Paper I and Lagarde et al. (2012, see these papers for details).

3.2. Rotation

We follow the evolution of the internal rotation profile from the zero age main sequence on, assuming initial solid body rotation, and an initial surface velocity of 75 km s^{-1} corresponding to 36% of the critical velocity (similar to Lagarde et al. 2012). We account for surface spin-down due to magnetic braking following the Kawaler (1988) formalism as described in Palacios et al. (2003) with a constant $K = 2\times10^{30}$.

Mass loss is included from the zero age main sequence following Reimers (1975) prescription with a parameter $\eta_\mathrm{R} = 0.5$ (see also Palacios et al. 2006). Rotation effects on mass loss are accounted for following Maeder & Meynet (2001). Angular momentum losses associated with mass loss are also accounted for, but anisotropy effects (see Maeder 2002) are neglected. However, because of the low-mass loss rate during the main sequence, these effects are negligible.

3.3. Wave excitation and spectrum along the main sequence evolution

As the only convective zone in the 1.1 $M_\odot$ main-sequence model is the envelope, we consider only waves generated by Reynolds stresses in this convective envelope. In the computations, we choose to multiply the kinetic energy flux obtained from the volumetric convective excitation by a factor of 5 in agreement with the results of Lecoanet & Quataert (2013) who show that the excitation by turbulent convection with a smooth transition at the radiative-convective transition leads to a flux about a factor of 5 higher than the one obtained by Eq. (15).

Figure 1 shows the luminosity spectrum of the IGWs generated by the convective envelope for the model at the age of 180 millions years. As already emphasized by Talon & Charbonnel (2005), the structure of the spectrum shows almost no variation along the main sequence. The left panel of Fig. 1 shows the spectrum of luminosity generated at the edge of the convective envelope. As already found by Talon & Charbonnel (2005), the waves which have the highest luminosity are those with small local frequency.

Moreover, as already pointed out by Talon & Charbonnel (2005) (see also Zahn et al. 1997), most of the waves are efficiently damped in the radiative region very close to the convective border. The central panels of Fig. 1 illustrate this point by showing the spectrum of wave luminosity at 0.05 $R_\odot$ below the convective border. At that depth, retrograde and prograde waves with high degree ℓ and small frequency are already damped, and this effect is more pronounced for the prograde waves with azimuthal degree $m = \ell$. For each frequency, and given degrees ℓ and m, the net luminosity is dominated by the retrograde waves where their maximum luminosity is limited to the area with small frequency and degree ℓ (see right panel of Fig. 1 and Eq. (12)).

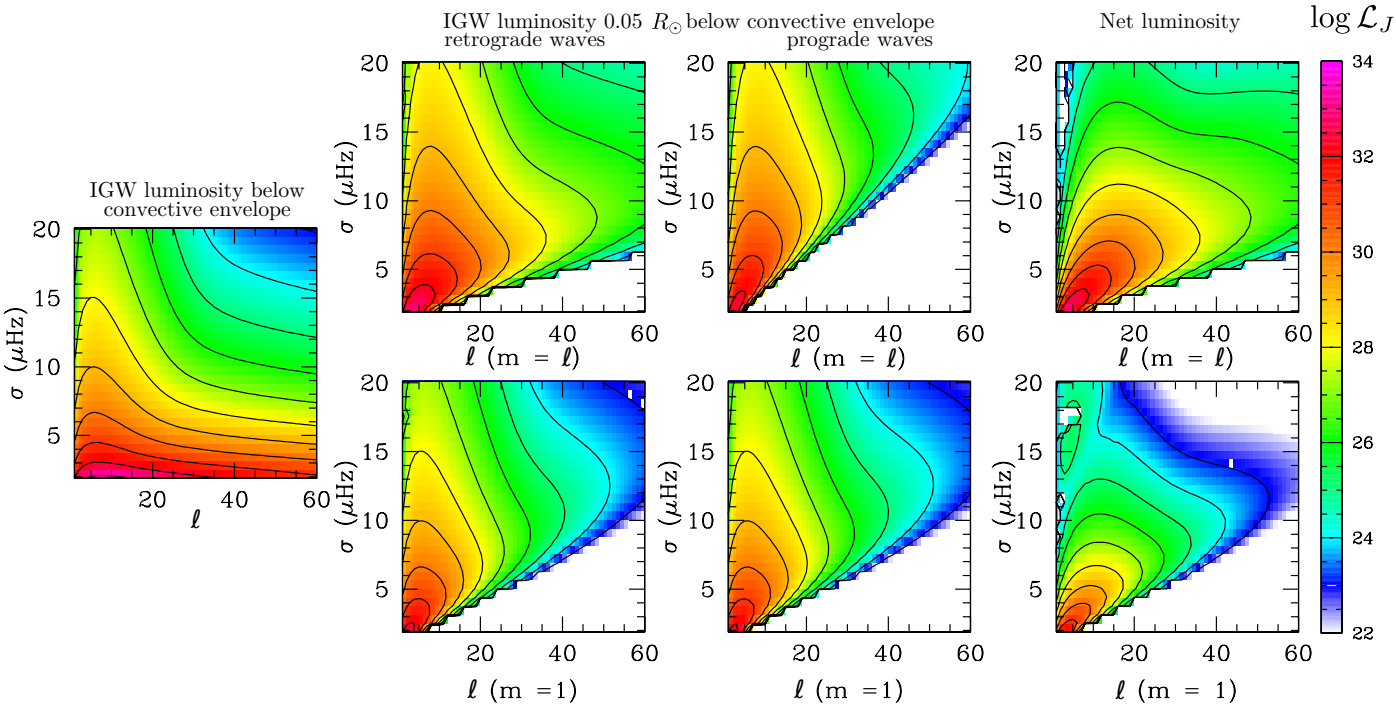

Fig. 1. *Left*: spectrum of the IGW luminosity generated by the convective Reynolds stresses of the envelope for various frequencies σ and degrees ℓ. *Middle*: spectrum of the IGW luminosity at 0.05 $R_\odot$ below the convective envelope for retrograde (*left*) and prograde (*right*) waves with various frequencies and degrees ℓ. Only the cases with $m = \ell$ (*top*) and $m = 1$ (*bottom*) are shown. *Right*: spectrum of the net luminosity at 0.05 $R_\odot$ below the convective envelope for various frequencies and degrees ℓ (and m).

4. Dynamical evolution of a 1.1 $M_\odot$ $Z_\odot$ star

In the following sections, we generalise the tools developed in Paper I to improve our understanding of the quantitative IGW effects on the transport of angular momentum and chemicals during the evolution of the 1.1 $M_\odot$ model along the main sequence.

4.1. Rotation

4.1.1. Internal rotation profiles

Figure 2 shows the evolution of the angular velocity profile between the zero age main sequence up to 382 million years where six extraction fronts have propagated to the surface. Talon & Charbonnel (2005) and Charbonnel & Talon (2005) explain that IGWs extract angular momentum at the depth they are damped. This depth moves toward the surface with time and then IGWs penetrate deeply into the star and a new extraction front starts. In our 1.1 $M_\odot$, we obtain a similar behaviour. In the following we will concentrate our analysis on the third extraction front to study the changes in rotation and chemical transport as it propagates toward the surface. The three curves in black, red, and green, correspond to the rotation profile at the three times located in Fig. 3 where the extraction front moves outward at $r = 0.15$, 0.3 and 0.5 $R_\odot$, respectively. Contrary to the general result obtained in the absence of IGWs (where only rotation, meridional circulation, and shear turbulence are taken into account) for a 1.1 $M_\odot$ star ($Z = Z_\odot$) and other solar-type star models, where we had a core spinning faster than the envelope (see e.g. Paper I), we obtain here a weak differential rotation because of its damping by IGWs and the related angular momentum extraction fronts (as in Talon & Charbonnel 2005).

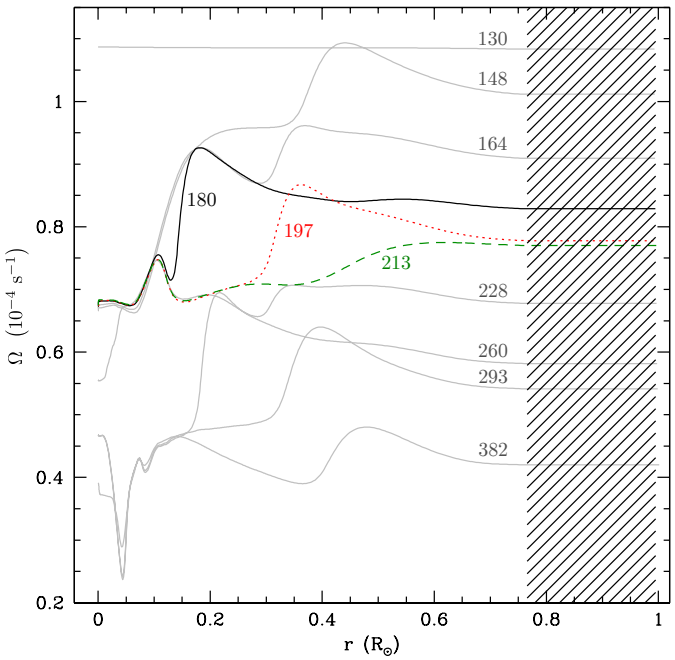

Fig. 2. Profiles of angular velocity in a 1.1 $M_\odot$ star ($Z = Z_\odot$) at different ages between 130 and 382 million years. The black, red, and green profiles at 180, 197, and 213 million years, respectively, indicate the time where we perform our analysis. Hatched area indicates the convective envelope.

4.1.2. Surface velocity

Figure 3 shows the evolution of the surface velocity for the first 2.5 Gyr on the main sequence (the central hydrogen abundance decreases from 0.71 to 0.44). The surface velocity starts on the

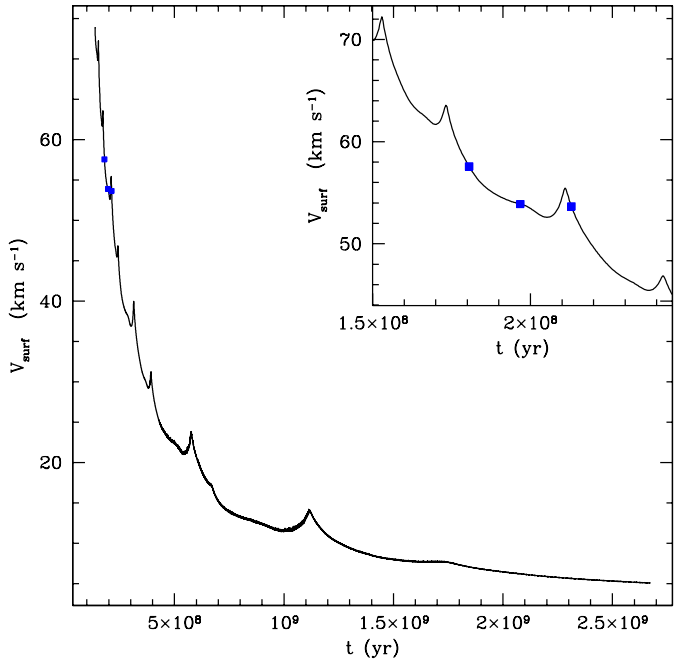

Fig. 3. Surface velocity of a 1.1 $M_\odot$ star ($Z = Z_\odot$), with an initial velocity of 75 km s^{-1} at the ZAMS. The bue squares at 180, 197, and 213 million years indicate the time at which the structures are detailed.

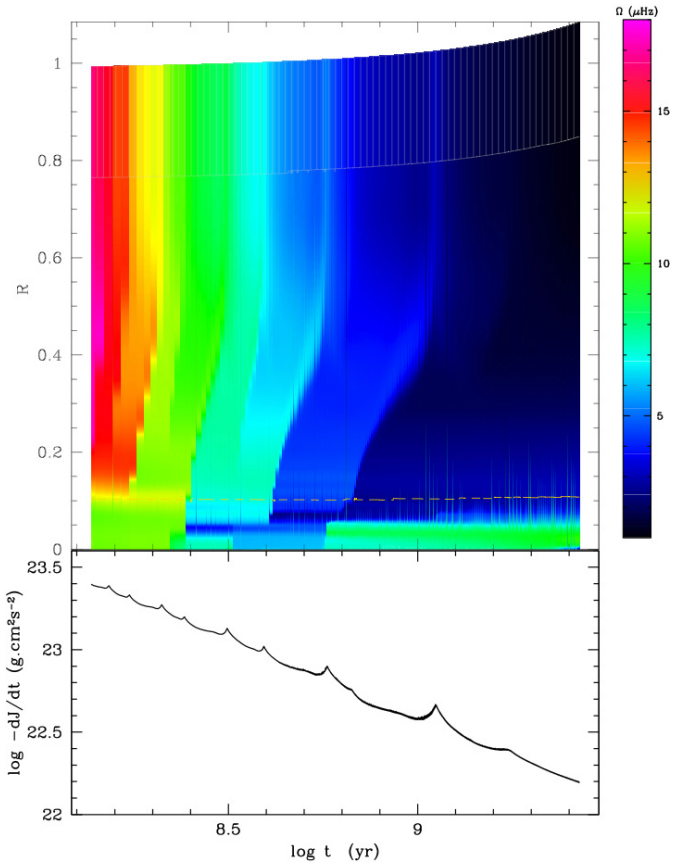

Fig. 4. *Top*: variation of the angular velocity ($\overline{\Omega}$) as a function of r during the computed evolution of the 1.1 $M_\odot$ star ($Z = Z_\odot$). The colour scale used allows the identification of the different fronts of extraction of the angular momentum and their propagation speed. The shaded area indicates the convective envelope, while the dotted white line corresponds to the limit of H-burning (defined as $\epsilon_{\rm nuc} \leq 1$ erg s^{-1}). *Bottom*: evolution of the loss of angular momentum during the computed evolution of the 1.1 $M_\odot$ star ($Z = Z_\odot$).

Zero-Age-Main-Sequence at 75 km s^{-1} and then it decreases because of magnetic braking to about 12−15 km s^{-1} at the Hyades ages, which is close to the velocity obtained by Gaige (1993) for star with a $T_{\rm eff}$ around 5980 K: $V_{\rm Hyades} = 8 \pm 10$ km s^{-1}. Thus the surface velocity reaches 5 km s^{-1} after 2.5 Gyr of evolution when most of the magnetic braking has occurred.

Along with this general decreasing trend, the surface velocity also shows a series of small peaks, which are due to the arrival at the surface of extraction fronts induced by the transport of angular momentum by IGWs (see Talon & Charbonnel 2005). In Fig. 4, we show the evolution of the rotation profile during the whole computed evolution, i.e. $\overline{\Omega}(r,t)$, along with the loss of angular momentum due to magnetic braking. Then, we can clearly identify the propagation of the different fronts of angular momentum extraction and their speed of propagation which becomes slower and slower as the star evolves. This is due to the strength of the magnetic wind and braking, which decreases with time. Therefore, less differential rotation between the convective envelope and the internal core is sustained. Then, the net bias between retrograde and prograde waves, which is fed by the differential rotation reservoir, becomes less and less pronounced and the efficiency of the extraction becomes less and less efficient and operates on longer time-scales.

In the following, we follow in detail the propagation of the third extraction front at three different times (180, 197, and 213 million years) indicated by the blue squares in Fig. 3.

4.2. Sustaining the meridional circulation

Figure 5 shows the two-dimensional reconstruction of the meridional circulation flows in the radiative interior. As in Paper I, they are represented in terms of the stream function ξ defined in Eq. (5). The striking difference with the models of 1.5 $M_\odot$ presented in Paper I computed without IGWs is the presence of numerous small loops of meridional circulation instead of having only two loops with a large one connecting the surface to the deep interior. As shown by Talon & Charbonnel (2003), the efficiency of IGWs is ruled by the size of the convective envelope, which becomes negligible for stars above ∼1.4 $M_\odot$. For lower mass stars IGWs need to be taken into account. Models of a 1.1 $M_\odot$ star without IGWs will show a similar pattern for the meridional circulation to the 1.5 $M_\odot$ star shown in Paper I. In the 1.1 $M_\odot$ star, where IGWs are taken into account, numerous loops of circulation are present with alternating clockwise and counterclockwise loops. As already noted by Talon & Charbonnel (2005), this meridional multi-loop pattern has a strong effect on the transport of angular momentum and chemicals that must be understood.

Figure 6 shows the reconstruction of the radial function of the vertical component of the meridional circulation (U_2) based on Eq. (22) obtained from the conservation of angular momentum, where U_Γ, U_V, and the $U_{\mathcal{L}_{\rm J}}$ represent the angular momentum extraction, the contribution of the shear, and of the one of Reynolds stresses caused by IGWs, respectively. We note that the contribution of IGWs is always positive (because of the net extraction of angular momentum) while the loops of meridional circulation have alternating positive and negative values. The propagation of the IGWs in the radiative interior and their damping create two main zones shown in Fig. 6. They are separated by the extraction front position at $r_{\rm extract} = 0.12, 0.3,$ and 0.5 $R_\odot$ in the three panels. Above (between the

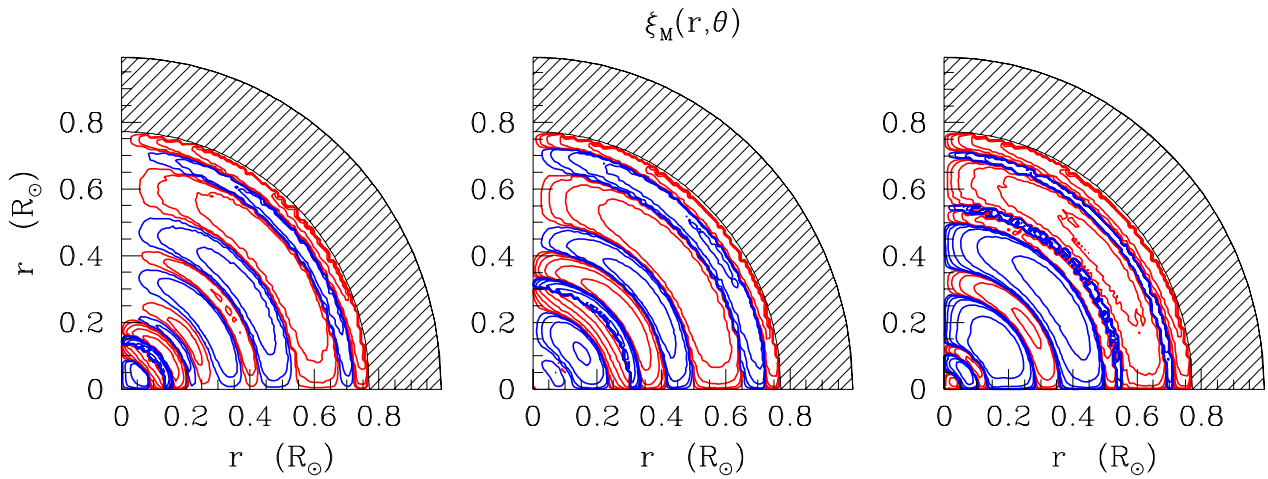

Fig. 5. Meridional circulation currents in a 1.1 $M_\odot$ star ($Z = Z_\odot$) model at 180 (*left*), 197 (*middle*), and 213 million years (*right*). Red and blue lines indicate counterclockwise and clockwise circulation, respectively. Hatched areas indicate the convective envelope.

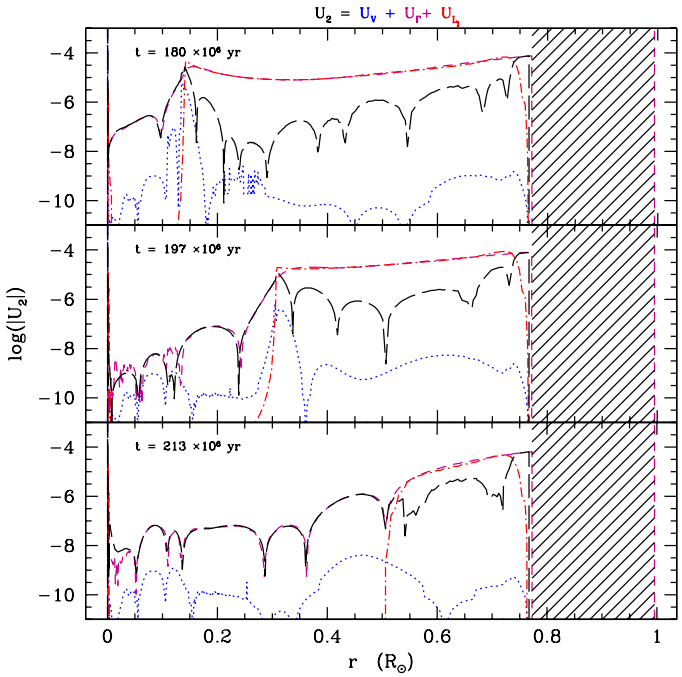

Fig. 6. Decomposition of the vertical component of the meridional circulation radial function U_2 for a 1.1 $M_\odot$ star ($Z = Z_\odot$) at three different epochs indicated in each panel. Black long dashed lines show the value of U_2, while red dashed-dotted, blue dotted, and magenta dashed lines indicate its different components $U_{\mathcal{L}_J}$, U_V and U_Γ, respectively (see Eq. (22)). Hatched areas indicate the convective envelope.

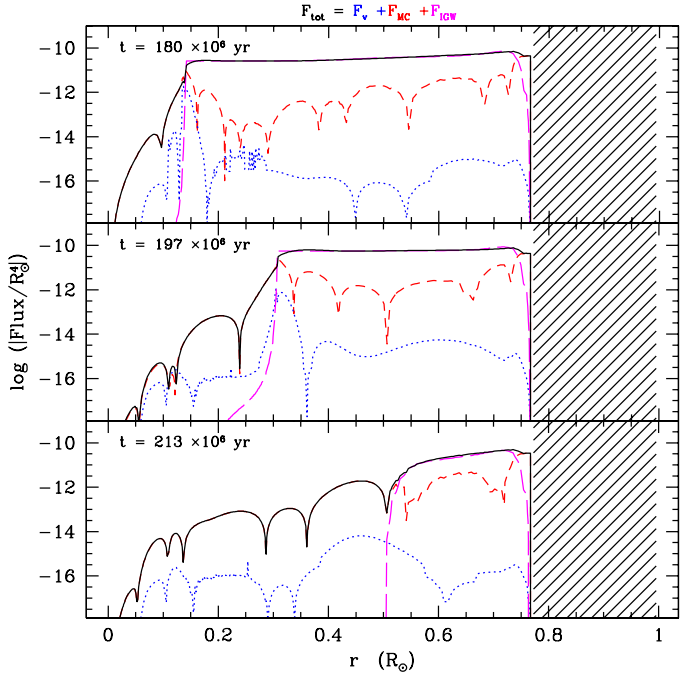

Fig. 7. Total flux of angular momentum ($F_{\rm tot}$, black solid line) decomposed into the contributions due to the meridional circulation ($F_{\rm MC}$, red dashed line), the shear-induced turbulence ($F_{\rm S}$, blue dotted line), and the Reynolds stresses caused by IGWs ($F_{\rm J}$, magenta dashed line) for a 1.1 $M_\odot$ star ($Z = Z_\odot$) at three different epochs indicated in each panel. Hatched areas indicate the convective envelope.

convective envelope and the region where they are damped $r \geq r_{\rm extract}$), the meridional circulation is sustained by the local variation of angular momentum given by U_Γ and by the Reynolds stresses caused by IGWs given by $U_{\mathcal{L}_J}$, i.e. $U_2 \approx U_\Gamma + U_{\mathcal{L}_J}$. Since U_Γ is negative while $U_{\mathcal{L}_J}$ is positive with the same order of magnitude, we are thus able to understand the meridional circulation radial function (U_2) amplitude, which can be alternatively positive and negative along the radius.

In the inner central part ($r < r_{\rm extract}$) where no IGWs are present because they have been damped near the extraction front, the meridional circulation is sustained mainly by the local variation of angular momentum given by U_Γ as in Paper I, i.e. $U_2 \approx U_\Gamma$.

The contribution of the shear (U_V) is always negligible owing to the nearly-flat profile of rotation. The only place where the shear increases sharply is around the extraction front. However, as the other components of the meridional circulation are also highly excited in this place, the shear never becomes important although the rotation profile displays a stronger differential profile there. However, at the end of the main sequence evolution, once the wind becomes weak, the transport of angular momentum by IGWs is less efficient with extraction fronts of

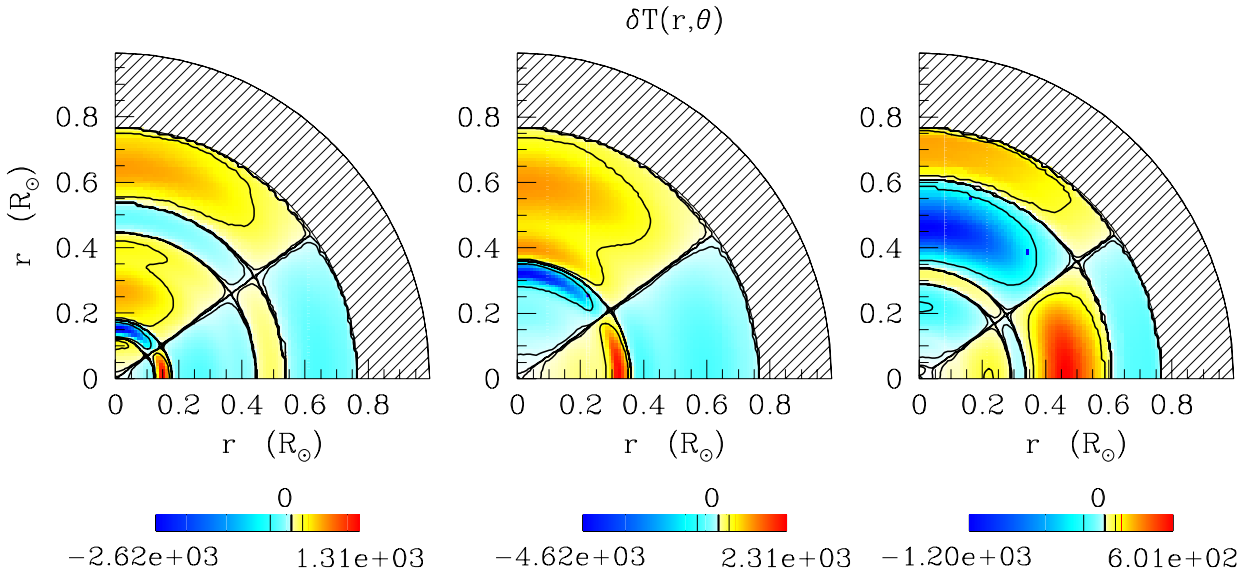

Fig. 8. Temperature fluctuation in the 1.1 $M_\odot$ star ($Z = Z_\odot$) model at 180 (*left*), 197 (*middle*) and 213 million years (*right*). Hatched areas indicate the convective envelope.

angular momentum that propagate more and more slowly (cf. Fig. 4). Then, once most of the angular momentum has been lost, a very weak meridional circulation is driven by the viscous stresses induced by the residual shear.

4.3. Flux of angular momentum

Here, we continue to examine the respective contribution of meridional circulation ($F_{\rm MC}$), shear ($F_{\rm S}$), and IGWs ($F_{\rm J}$) to the total flux of angular momentum by looking at the fluxes carried by these three processes. Our analysis is presented in Fig. 7 for the three chosen structures of the propagation of the extraction front. We retrieve the similar pattern as in Fig. 6 where the radiative region can be decomposed into two regimes. In the inner one, below the extraction front ($r < r_{\rm extract}$), the transport of angular momentum is dominated by its advection by the meridional circulation, while above ($r \geq r_{\rm extract}$), IGWs are the main conveyor. In the whole radiation zone, the diffusion of angular momentum by the shear-induced turbulence remains a secondary process.

Near the extraction front, the meridional circulation presents two important characteristics: a high value of its velocity and a double inversion peak (see Fig. 5) as a pattern with three fixed loops are present between 0.09–0.22, 0.18–0.42, and 0.5–0.68 $R_\odot$ in the right, middle, and left panel, respectively. The two inner loops bring angular momentum from the outside to the extraction front while the outer one transports angular momentum outward. This typical pattern is responsible for the peak seen in the profile of angular momentum near the extraction front.

Moreover, as shown in Fig. 2, the profile of $\overline{\Omega}$ is frozen in the region below the extraction front. This behaviour can be understood as follows. First, the amplitude of the angular momentum flux stays almost constant where IGWs are the main conveyor. Thus, angular momentum is efficiently extracted from the front to the convective envelope and hence this process moves the front to higher radius. Second, in the inner part, the total flux drops by several orders of magnitude compared to the region above and the succession of clockwise and counterclockwise loops of meridional circulation halts the transport of angular momentum. The net effect of these two mechanisms freezes the evolution of angular momentum in the inner part compared to the time needed by the front to move toward the surface.

4.4. Entropy transport

Figure 8 displays the two-dimensional reconstruction of the temperature perturbation (δT) in the meridional plane at different ages along the evolution. Its behaviour is closely related to the gradients of angular momentum; near the extraction front where steep gradients occur, δT presents its maximum values. Furthermore, the value of the perturbations always remains small as $\delta T/\overline{T}$ is lower than 0.1%. This result validates our perturbation analysis.

Figure 9 (both panels) depicts how the thermal relaxation in the heat transport equation is achieved. In Paper I, we showed that in the absence of IGWs the advection of entropy by the meridional circulation ($\widetilde{\mathcal{T}}_{\rm Adv}$) is compensated both by the thermal ($\widetilde{\mathcal{T}}_{\rm Th}$) and barotropic ($\widetilde{\mathcal{T}}_{\mathcal{B}}$) components of the radiative flux. The situation is quite different with the presence of IGWs because the main peak of entropy advection by the meridional circulation (see Fig. 6) near the extraction front is solely balanced by the thermal component. In the last panel of Fig. 9 (top), the heat transport is weak and all the components have small values because the front we are following arrives at the surface and a new one will be created. The bottom panel of Fig. 9 shows the different components of the heat transport equation with a zoom in the region outside the extraction front. There, the advection of heat by the meridional circulation is still balanced by the thermal component. However, the barotropic component induces some modulation. The nuclear and gravitational energy generation term ($\widetilde{\mathcal{T}}_{\rm N-G}$) plays a role only in the central region below 0.1–0.2 $R_\odot$. Finally, the non-stationary term ($\widetilde{\mathcal{T}}_{\rm NS}$) is negligible as it is mainly sensitive to the structural changes of the star, which remain small during the main sequence.

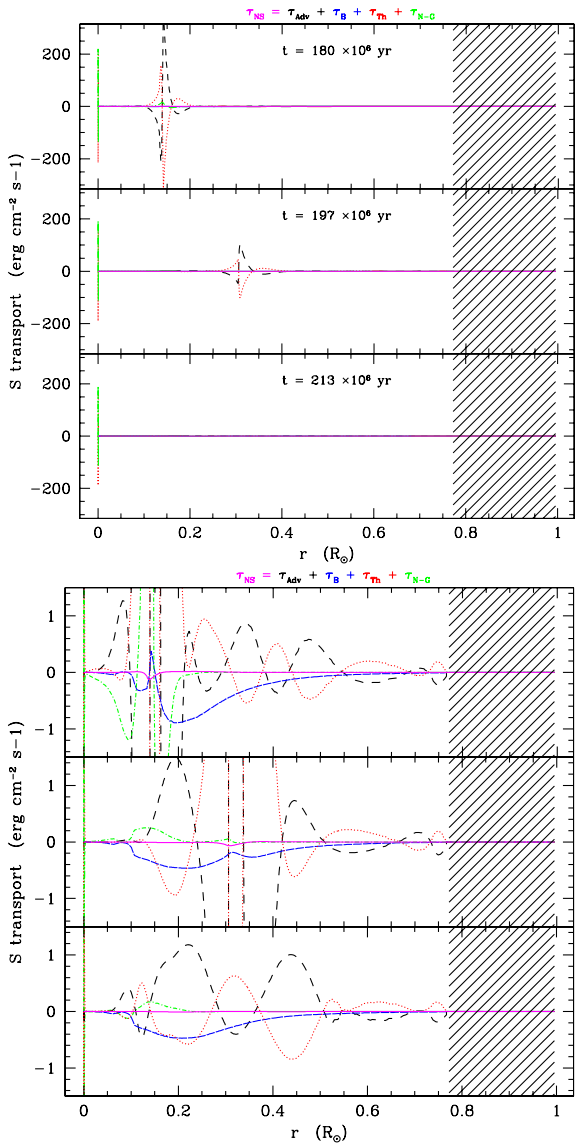

Fig. 9. *Upper panels*: heat transport for a 1.1 $M_\odot$ star ($Z = Z_\odot$) at three different epochs indicated in each panel with the terms non-stationary ($\widetilde{\mathcal{T}}_{\rm NS}$; magenta solid line), barotropic ($\widetilde{\mathcal{T}}_{\mathcal{B}}$; blue dashed line), baroclinic ($\widetilde{\mathcal{T}}_{\rm Th}$; red dotted line), and advective ($\widetilde{\mathcal{T}}_{\rm Adv}$; black long dashed line), and the contribution due to nuclear and gravitational energy variations ($\widetilde{\mathcal{T}}_{\rm N-G}$; green dashed-dotted line). *Lower panels*: similar to the upper panel with a zoom on the small amplitude components. Hatched areas indicate the convective envelope.

4.5. Effects on chemicals

4.5.1. Horizontal chemical unbalance

Figure 10 displays the two-dimensional reconstruction of horizontal fluctuations of mean molecular weight (μ). Nuclear burning increases the mean molecular weight in the centre and creates a negative vertical gradient. Then, the meridional circulation creates horizontal gradients when clockwise loops bring matter with low μ from the outside near the equatorial plane and push high μ matter along the pole from the centre to the outer regions. The reverse happens with counterclockwise loops. These μ perturbations tend to be erased by the horizontal turbulence.

Because of the numerous loops of meridional circulation we would expect the behaviour of the μ perturbations to be erratic. While Fig. 10 mainly confirms it, we can still identify some long-lived patterns. We see that the inner μ perturbations located at $r = 0.10\ R_\odot$ remain at the three times. This comes from the initial μ perturbations that are protected by clockwise loops that stay at this radius at all three times (see Fig. 5). Furthermore, as the horizontal diffusion is also weaker near the stellar centre (see Fig. 11), the initial μ perturbation is eroded on a longer timescale while the pattern above 0.10 $R_\odot$ changed more rapidly.

4.5.2. Transport of chemicals

Figure 11 compares the diffusion coefficients of the various processes that act on the transport of chemicals. First, the horizontal turbulent transport is stronger than the vertical (i.e. $D_{\rm H} \gg D_{\rm V}$) as expected from the shellular rotation hypothesis. Then, because of the very little vertical gradient of angular velocity, the vertical shear is weak except near the extraction front. The effective diffusion by meridional circulation and horizontal turbulence ($D_{\rm eff}$) follows the loops of the circulation. Therefore, the net effect is a strong reduction of the vertical mixing compared to the model presented in Paper I. Similar results have been obtained by Talon & Charbonnel (2005). These differences in the diffusion coefficient lead to a lower efficiency of the transport of light elements like Li near the convective envelope. As shown by Talon & Charbonnel (2003), gravity waves can inhibit the Li depletion on the cool side of the Li dip observed in open clusters (see e.g. Burkhart & Coupry 2000).

5. Conclusions and perspectives

In this article, we generalised the work in Paper I aimed at unravelling secular transport and mixing processes in stellar radiation zones during the main sequence taking IGW actions into account. Using the STAREVOL code where the formalisms by Mathis & Zahn (2004) and Talon & Charbonnel (2005) are implemented, we simulated the evolution of a 1.1 $M_\odot$, $Z_\odot$ star focussing on the highly non-linear interaction between differential rotation, large-scale meridional circulation, shear-induced turbulence and IGWs. In our work, the non-diffusive character of angular momentum transport by the meridional circulation and IGWs is preserved. Then, using our generalised diagnoses, we identify that the meridional flows are driven by the external torque applied on the stellar surface by stellar winds and by IGWs and viscous stresses rather than by thermal imbalance (see also Busse 1982; Rieutord 2006) (stellar structure adjustments are also important, but not on the evolution phases we have studied in this work). This precise analysis now allows us to explain the highly multi-cellular meridional circulation already identified by Talon & Charbonnel (2005) and shows that the usual Eddington-Sweet vision of this flow must be abandoned. We note that this forcing of mean meridional and zonal flows by IGWs also occurs in the atmosphere of the Earth and the other planets (e.g. Holton 1982; Fritts & Alexander 2003). We then clarified the precise way IGWs act on the large-scale dynamics for angular momentum, heat, and chemical transports.

First, as in Talon & Charbonnel (2005), we unraveled the dynamics of angular momentum extraction fronts that propagate from the centre to the surface of the star. We note that the velocity of their propagation decreases along the evolution of the star during which surface braking by stellar winds becomes less efficient. Indeed, the corresponding applied torque sustains the differential rotation between the convective envelope of the star and its radiative core. This feeds the IGW action because of the different Doppler-shift of pro- and retrograde waves from which a net transport of angular momentum results. Then, once most

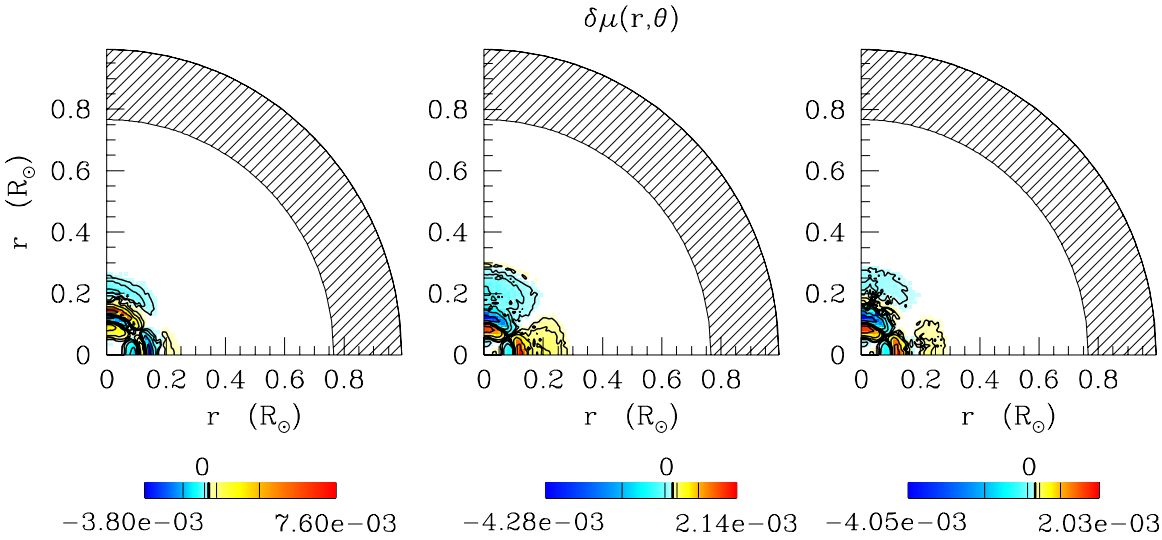

Fig. 10. Two-dimensional reconstruction of the μ fluctuations in the 1.1 $M_\odot$ star ($Z = Z_\odot$) model at 180 (*left*), 197 (*middle*), and 213 million years (*right*). Hatched areas indicate the convective envelope.

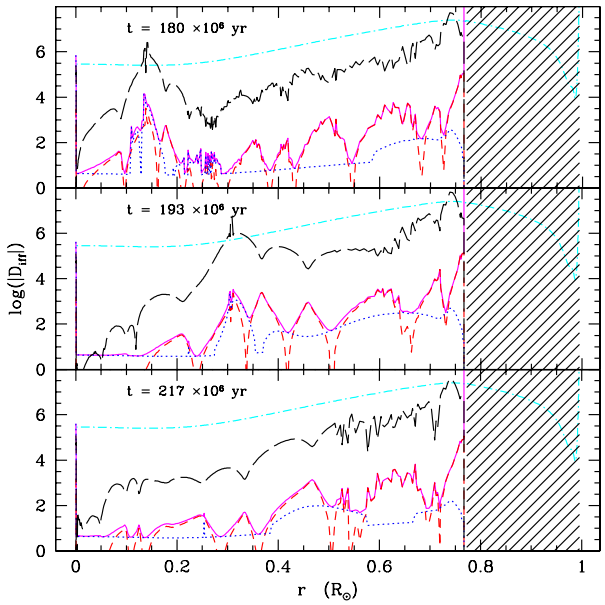

Fig. 11. Profiles of the thermal diffusivity (K; cyan dashed-dotted lines), and the diffusion coefficient associated with the meridional circulation ($D_{\rm eff}$; red dashed lines), and with the horizontal ($D_{\rm H}$; black long dashed lines) and vertical turbulence ($D_{\rm V}$; blue dotted lines) for a 1.1 $M_\odot$ star ($Z = Z_\odot$) at three different epochs indicated in each panel. The total diffusion coefficient used for the mixing of chemicals is indicated with magenta full lines. Hatched areas indicate the convective envelope.

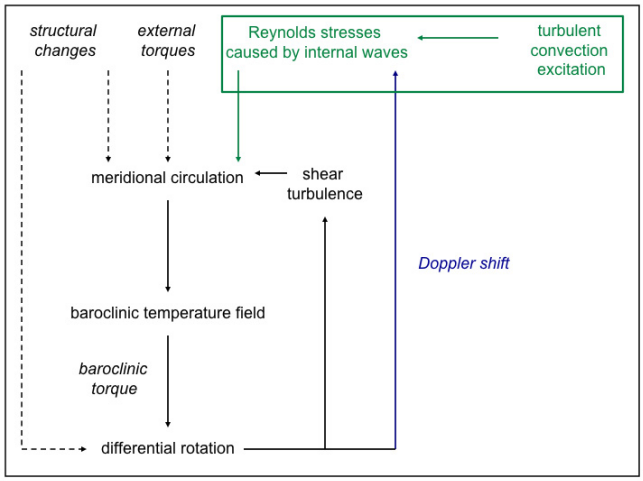

Fig. 12. Secular hydrodynamics of stellar radiation zones taking into account IGWs actions (here, in the green box). The action of differential rotation through the Doppler shift is represented in blue.

of the differential rotation has been damped, a very weak meridional circulation is driven by the viscous stresses induced by the residual shear as described in Paper I. Next, heat and chemical transports are strongly affected by IGW action because of the related modification of the meridional circulation behaviour. Then, the meridional circulation advects entropy (and chemicals) and the star relaxes into a new thermal state. This in turn generates a new differential rotation profile because of the induced baroclinic torque (see Eq. (33)) and the related thermal wind (see Fig. 12).

The main improvments that should be added to this work in the near future mainly consist of improvments in the treatment of the excitation, propagation, and damping of IGWs.

First, for IGW amplitude, we here assume the prescription given by Kumar & Quataert (1997) for their volumetric stochastic excitation. However, progress has been achieved both analytically (Belkacem et al. 2009; Samadi et al. 2010) and using non-linear numerical simulations (Kiraga et al. 2005; Browning et al. 2004; Dintrans et al. 2005; Rogers & Glatzmaier 2005, 2006; Brun et al. 2011; Alvan et al. 2012) for the volumetric excitation and the surface excitation due to turbulent plumes. In the near future, it will thus be particularly important to extract usable prescriptions for excited IGW spectra from these works and to implement it in STAREVOL. Furthermore, as in the present implementation, it will be important to have appropriate prescriptions for each evolution phase where convective region properties evolve (see Talon & Charbonnel 2008; Charbonnel et al. 2013).

Next, we have ignored the action of the Coriolis acceleration and the Lorentz force (due to the dynamo field at the level of the excitation region at convection/radiation borders and/or to a fossil field in the bulk of stellar radiation zones) on IGWs. Both rotation and magnetic fields modify their propagation and

damping, as well as the related transport of angular momentum and mixing, particularly for IGWs that are excited with frequencies close to the inertial frequency (2Ω) and to the Alfvén frequency (see Pantillon et al. 2007; Mathis et al. 2008a; Mathis 2009) for the action of the Coriolis acceleration and Mathis & de Brye (2011, 2012) for the combined action of rotation and magnetic fields); for example, equatorial trappings occur for these low-frequency IGWs. However, as has been demonstrated by Mathis & de Brye (2012), the net bias between pro- and retrograde waves that leads to the efficient extraction of angular momentum in solar-type stars by IGWs is conserved even when both the Coriolis acceleration and the Lorentz force are taken into account. It will be thus important to implement, step by step, their action on IGWs to get the complete interaction between IGWs and the large-scale dynamical processes in stellar radiation regions.

Finally, the torques applied at the surface of the star have an important impact on the internal transport processes. If the prescription by Kawaler (1988) is adopted here, it will be important to improve the prescriptions used for this torque, for example using the prescriptions obtained from three-dimensional simulations of stellar winds where the dependence of the wind on the rotation rate of the star is taken into account (Matt et al. 2012).

All of these theoretical improvments of our vision of the dynamical evolution of stars will benefit from constraints coming from seismology and surface abundance observations of the whole Hertzsprung-Russell diagram.

Acknowledgements. T.D. and C.C. acknowledge financial support from the Swiss National Science Foundation (FNS) and from ESF-Eurogenesis. This work was also supported by the French Programme National de Physique Stellaire (PNPS) of CNRS/INSU, by the CNES-SOHO/GOLF grant and asteroseismology support in CEA-Saclay, and by the TOUPIES project funded by the French National Agency for Research (ANR). S.M. is grateful to Geneva Observatory where part of this work has been realized.

Appendix A: Meridional circulation and angular momentum transport

We consider Eq. (16) for the mean angular momentum transport

$$\overline{\rho}\frac{\mathrm{d}}{\mathrm{d}t}\left(r^2\overline{\Omega}\right) = \frac{1}{5r^2}\partial_r\left(\overline{\rho}r^4\overline{\Omega}U_2\right) + \frac{1}{r^2}\partial_r\left(\overline{\rho}\nu_V r^4\partial_r\overline{\Omega}\right) - \frac{3}{8\pi}\frac{1}{r^2}\partial_r\mathcal{L}_J(r) \tag{39}$$

that takes IGW action into account. We integrate it over a spherical shell

$$\int_{r=r_1}^{r=r_2}\overline{\rho}r'^2\frac{\mathrm{d}}{\mathrm{d}t}\left(r'^2\overline{\Omega}\right)\mathrm{d}r' = \frac{1}{5}\int_{r=r_1}^{r=r_2}\partial_{r'}\left(\overline{\rho}r'^4\overline{\Omega}U_2\right)\mathrm{d}r' + \int_{r=r_1}^{r=r_2}\partial_{r'}\left(\overline{\rho}\nu_V r'^4\partial_r\overline{\Omega}\right)\mathrm{d}r' - \frac{3}{8\pi}\int_{r=r_1}^{r=r_2}\partial_r\mathcal{L}_J(r')\,\mathrm{d}r', \tag{40}$$

where r_1 and r_2 are, respectively, its inner and outer radius. Introducing the elementary mass element $\mathrm{d}m = 4\pi\overline{\rho}r^2\mathrm{d}r$, we obtain

$$\frac{1}{4\pi}\int_{m=m(r_1)}^{m=m(r_2)}\frac{\mathrm{d}}{\mathrm{d}t}\left(r'^2\overline{\Omega}\right)\mathrm{d}m = \frac{1}{5}\left[\left(\overline{\rho}r^4\overline{\Omega}U_2\right)_{r=r_2} - \left(\overline{\rho}r^4\overline{\Omega}U_2\right)_{r=r_1}\right] + \left[\left(\overline{\rho}\nu_V r^4\partial_r\overline{\Omega}\right)_{r=r_2} - \left(\overline{\rho}\nu_V r^4\partial r\overline{\Omega}\right)_{r=r_1}\right] - \frac{3}{8\pi}\left[\mathcal{L}_J(r=r_2) - \mathcal{L}_J(r=r_1)\right]. \tag{41}$$

We apply the following identity

$$\frac{\mathrm{d}}{\mathrm{d}t}\left[\int_{m_1(t)}^{m_2(t)}f(m,t)\mathrm{d}m\right] = \int_{m_1(t)}^{m_2(t)}\frac{\mathrm{d}}{\mathrm{d}t}\left[f(m,t)\right]\mathrm{d}m + \left\{\frac{\mathrm{d}m_2(t)}{\mathrm{d}t}f(m_2,t) - \frac{\mathrm{d}m_1(t)}{\mathrm{d}t}f(m_1,t)\right\}.$$

In our Lagrangian description, the mass is conserved, i.e. $\frac{\mathrm{d}m_2(t)}{\mathrm{d}t} = \frac{\mathrm{d}m_1(t)}{\mathrm{d}t} = 0$, so

$$\frac{1}{4\pi}\frac{\mathrm{d}}{\mathrm{d}t}\left[\int_{m=m(r_1)}^{m=m(r_2)}r'^2\overline{\Omega}\mathrm{d}m\right] = \frac{1}{5}\left[\left(\overline{\rho}r^4\overline{\Omega}U_2\right)_{r=r_2} - \left(\overline{\rho}r^4\overline{\Omega}U_2\right)_{r=r_1}\right] + \left[\left(\overline{\rho}\nu_V r^4\partial_r\overline{\Omega}\right)_{r=r_2} - \left(\overline{\rho}\nu_V r^4\partial_r\overline{\Omega}\right)_{r=r_1}\right] - \frac{3}{8\pi}\left[\mathcal{L}_J(r=r_2) - \mathcal{L}_J(r=r_1)\right]. \tag{42}$$

Finally, to obtain the value of the radial function of the vertical component of the meridional circulation at $m(r)$, we set $r_1 = 0$ and $r_2 = r$ that leads to

$$U_2 = \frac{5}{\overline{\rho}r^4\overline{\Omega}}\left[\Gamma(m) - \overline{\rho}\nu_V r^4\partial_r\overline{\Omega} + \frac{3}{8\pi}\mathcal{L}_J(r)\right], \tag{43}$$

where

$$\Gamma(m) = \frac{1}{4\pi}\frac{\mathrm{d}}{\mathrm{d}t}\left[\int_0^{m(r)}r'^2\overline{\Omega}\mathrm{d}m'\right]. \tag{44}$$

Appendix B: $\mathcal{T}_2$ components of the heat transport equation

This is an advection/diffusion equation, where the advective term associated with the meridional circulation caused by the transport of angular momentum plays the role of a source or sink of heat. The terms $\mathcal{T}_{2,\mathrm{Th}}$ and $\mathcal{T}_{2,\mathcal{B}}$ describe the usual spherical diffusion of heat and the component of the divergence of the radiative flux due to the flattening of the isobar by the centrifugal acceleration; $\boldsymbol{\nabla}\cdot\boldsymbol{F}_{\mathrm{H}}$ is the entropy flux carried by the horizontal turbulence. Finally, $\mathcal{T}_{2,\mathrm{N-G}}$ corresponds to the coupling with the nuclear energy generation. Their derivation may be found in Decressin et al. (2009) and we obtain the thermic term

$$\mathcal{T}_{2,\mathrm{Th}} = \frac{\rho_m}{\overline{\rho}}\left[\frac{r}{3}\partial_r\mathcal{A}_2(r) - \frac{2H_T}{3r}\left(1+\frac{D_{\mathrm{H}}}{K}\right)\frac{\widehat{T}_2}{\overline{T}}\right],$$

the barotropic term

$$\mathcal{T}_{2,\mathcal{B}} = \frac{2}{3}\left[1 - \frac{\overline{\Omega}^2}{2\pi G\overline{\rho}} - \frac{2}{3}\frac{\rho_m}{\rho}\left(\phi\frac{\widehat{\mu}_2}{\overline{\mu}} - \delta\frac{\widehat{T}_2}{\overline{T}}\right) - \frac{\left(\overline{\epsilon}+\overline{\epsilon}_{\mathrm{grav}}\right)}{\epsilon_m}\right]\overline{\Omega}^2\partial_r\left(\frac{r^2}{\overline{g}}\right) - \frac{2}{3}\frac{\rho_m}{\overline{\rho}}\left(\phi\frac{\widehat{\mu}_2}{\overline{\mu}} - \delta\frac{\widehat{T}_2}{\overline{T}}\right),$$

and the term associated with local energy sources

$$\mathcal{T}_{2,\mathrm{N-G}} = \frac{\left(\overline{\epsilon}+\overline{\epsilon}_{\mathrm{grav}}\right)}{\epsilon_m}\left[\mathcal{A}_2(r) + \left(f_\epsilon\epsilon_T - f_\epsilon\delta + \delta\right)\frac{\widehat{T}_2}{\overline{T}} + \left(f_\epsilon\epsilon_\mu + f_\epsilon\phi - \phi\right)\frac{\widehat{\mu}_2}{\overline{\mu}}\right],$$

where

$$\mathcal{A}_2(r) = H_T \partial_r \left(\frac{\widehat{T}_2}{\overline{T}} \right) - (1 - \delta + \chi_T) \frac{\widehat{T}_2}{\overline{T}} - \left(\phi + \chi_\mu \right) \frac{\widehat{\mu}_2}{\overline{\mu}} \tag{45}$$

and L and M have their usual meanings. We have introduced the temperature scale-height $H_T = \left| \mathrm{d}r / \mathrm{d} \ln \overline{T} \right|$, the horizontal eddy-diffusivity D_H and $f_\epsilon = \overline{\epsilon} / \left(\overline{\epsilon} + \overline{\epsilon}_\mathrm{grav} \right)$, with $\overline{\epsilon}$ and $\overline{\epsilon}_\mathrm{grav}$ being the mean nuclear and gravitational energy release rates, respectively; $\epsilon_\mu = (\partial \ln \overline{\epsilon} / \partial \ln \overline{\mu})_{\overline{P},\overline{T}}$ and $\chi_\mu = (\partial \ln \chi / \partial \ln \overline{\mu})_{\overline{P},\overline{T}}$ are the logarithmic derivatives of $\overline{\epsilon}$ and of the radiative conductivity χ with respect to $\overline{\mu}$, and $\epsilon_T = \left(\partial \ln \overline{\epsilon} / \partial \ln \overline{T} \right)_{\overline{P},\overline{\mu}}$ and $\chi_T = \left(\partial \ln \chi / \partial \ln \overline{T} \right)_{\overline{P},\overline{\mu}}$ are the derivatives of these same quantities with respect to $\overline{T}$; $\epsilon_m = L/M$ and $\rho_m = 3\overline{g}(r)/4\pi r G$ are the horizontal average of the energy production rate and the mean density inside the considered isobar. Finally, the signature of mixing induced by transport processes, i.e. the fluctuation of the mean molecular weight $\delta\mu(\boldsymbol{r}, t) = \widehat{\mu}_2(r, t) P_2(\cos\theta)$, has been introduced.

References

Aerts, C., Thoul, A., Daszyńska, J., et al. 2003, Science, 300, 1926
Alvan, L., Brun, A. S., & Mathis, S. 2012, in SF2A-2012: Proceedings of the Annual meeting of the French Society of Astronomy and Astrophysics, eds. S. Boissier, P. de Laverny, N. Nardetto, et al., 289
Beck, P. G., Montalban, J., Kallinger, T., et al. 2012, Nature, 481, 55
Belkacem, K., Samadi, R., Goupil, M. J., et al. 2009, A&A, 494, 191
Bouvier, J. 2008, A&A, 489, L53
Browning, M. K., Brun, A. S., & Toomre, J. 2004, ApJ, 601, 512
Brun, A. S., Miesch, M. S., & Toomre, J. 2011, ApJ, 742, 79
Burkhart, C., & Coupry, M. F. 2000, A&A, 354, 216
Busse, F. H. 1982, ApJ, 259, 759
Ceillier, T., Eggenberger, P., García, R. A., & Mathis, S. 2012, Astron. Nachr., 333, 971
Chaboyer, B., & Zahn, J.-P. 1992, A&A, 253, 173
Decressin, T., Baumgardt, H., Kroupa, P., Meynet, G., & Charbonnel, C. 2009a, in The ages of stars, ed. D. Soderblom, IAU Symp., 258
Charbonnel, C., & Talon, S. 2005, Science, 309, 2189
Charbonnel, C., Decressin, T., Amard, L., Palacios, A., & Talon, S. 2013, A&A, 554, A40
Decressin, T., Mathis, S., Palacios, A., et al. 2009b, A&A, 495, 271
Deheuvels, S., García, R. A., Chaplin, W. J., et al. 2012, ApJ, 756, 19
Dintrans, B., Brandenburg, A., Nordlund, Å., & Stein, R. F. 2005, A&A, 438, 365
Eff-Darwich, A., & Korzennik, S. G. 2012, Sol. Phys., 149
Eggenberger, P., Maeder, A., & Meynet, G. 2005, A&A, 440, L9
Eggenberger, P., Meynet, G., Maeder, A., et al. 2008, Ap&SS, 316, 43
Eggenberger, P., Montalbán, J., & Miglio, A. 2012, A&A, 544, L4
Espinosa Lara, F., & Rieutord, M. 2007, A&A, 470, 1013
Fritts, D. C., & Alexander, M. J. 2003, Rev. Geophys., 41, 1003
Gaige, Y. 1993, A&A, 269, 267
Garaud, P., & Garaud, J.-D. 2008, MNRAS, 391, 1239
García, R. A., Turck-Chièze, S., Jiménez-Reyes, S. J., et al. 2007, Science, 316, 1591
Garcia Lopez, R. J., & Spruit, H. C. 1991, ApJ, 377, 268
Goldreich, P., & Kumar, P. 1990, ApJ, 363, 694
Goldreich, P., & Nicholson, P. D. 1989, ApJ, 342, 1075
Goldreich, P., Murray, N., & Kumar, P. 1994, ApJ, 424, 466
Gough, D. O., & McIntyre, M. E. 1998, Nature, 394, 755
Heger, A., Langer, N., & Woosley, S. E. 2000, ApJ, 528, 368
Holton, J. R. 1982, J. Atmos. Sci., 39, 791
Irwin, J., & Bouvier, J. 2009, in IAU Symp. 258, eds. E. E. Mamajek, D. R. Soderblom, & R. F. G. Wyse, 363
James, D. J., Barnes, S. A., Meibom, S., et al. 2010, A&A, 515, A100
Kawaler, S. D. 1988, ApJ, 333, 236
Kawaler, S. D. 2004, in IAU Symp., 215, Stellar Rotation, eds. A. Maeder, & P. Eenens, 561
Kippenhahn, R., & Weigert, A. 1990, Stellar Structure and Evolution, Astronomy and Astrophysics Library (Berlin, Heidelberg, New York: Springer-Verlag)
Kiraga, M., Jahn, K., Stępień, K., & Zahn, J.-P. 2003, Acta Astron., 53, 321
Kiraga, M., Stepien, K., & Jahn, K. 2005, Acta Astron., 55, 205
Kumar, P., & Quataert, E. J. 1997, ApJ, 475, L143
Kumar, P., Talon, S., & Zahn, J.-P. 1999, ApJ, 520, 859
Lagarde, N., Decressin, T., Charbonnel, C., et al. 2012, A&A, 543, A108
Lai, D. 2012, MNRAS, 423, 486
Lecoanet, D., & Quataert, E. 2013, MNRAS, 430, 2363
MacGregor, K. B., & Charbonneau, P. 1999, ApJ, 519, 911
Maeder, A. 1997, A&A, 321, 134
Maeder, A. 2002, A&A, 392, 575
Maeder, A. 2003, A&A, 399, 263
Maeder, A. 2009, Physics, Formation and Evolution of Rotating Stars
Maeder, A., & Meynet, G. 2000, A&A, 361, 159
Maeder, A., & Meynet, G. 2001, A&A, 373, 555
Maeder, A., & Zahn, J.-P. 1998, A&A, 334, 1000
Maeder, A., Meynet, G., Lagarde, N., & Charbonnel, C. 2013, A&A, 553, A1
Marques, J. P., Goupil, M. J., Lebreton, Y., et al. 2013, A&A, 549, A74
Mathis, S. 2009, A&A, 506, 811
Mathis, S., & de Brye, N. 2011, A&A, 526, A65
Mathis, S., & de Brye, N. 2012, A&A, 540, A37
Mathis, S., & Zahn, J.-P. 2004, A&A, 425, 229
Mathis, S., & Zahn, J.-P. 2005, A&A, 440, 653
Mathis, S., Palacios, A., & Zahn, J.-P. 2004, A&A, 425, 243
Mathis, S., Talon, S., Pantillon, F.-P., & Zahn, J.-P. 2008a, Sol. Phys., 251, 101
Mathur, S., Eff-Darwich, A., García, R. A., & Turck-Chièze, S. 2008, A&A, 484, 517
Matt, S. P., MacGregor, K. B., Pinsonneault, M. H., & Greene, T. P. 2012, ApJ, 754, L26
Meibom, S., Mathieu, R. D., & Stassun, K. G. 2009, ApJ, 695, 679
Meibom, S., Mathieu, R. D., Stassun, K. G., Liebesny, P., & Saar, S. H. 2011, ApJ, 733, 115
Mestel, L., & Weiss, N. O. 1987, MNRAS, 226, 123
Meynet, G., & Maeder, A. 2000, A&A, 361, 101
Meynet, G., Eggenberger, P., & Maeder, A. 2011, A&A, 525, L11
Mosser, B., Goupil, M. J., Belkacem, K., et al. 2012, A&A, 548, A10
Ogilvie, G. I., & Lin, D. N. C. 2007, ApJ, 661, 1180
Palacios, A., Talon, S., Charbonnel, C., & Forestini, M. 2003, A&A, 399, 603
Palacios, A., Charbonnel, C., Talon, S., & Siess, L. 2006, A&A, 453, 261
Pantillon, F. P., Talon, S., & Charbonnel, C. 2007, A&A, 474, 155
Pinsonneault, M. 1997, ARA&A, 35, 557
Pinsonneault, M. H., Kawaler, S. D., Sofia, S., & Demarque, P. 1989, ApJ, 338, 424
Pinto, R. F., Brun, A. S., Jouve, L., & Grappin, R. 2011, ApJ, 737, 72
Prat, V., & Lignières, F. 2013, A&A, 551, L3
Reimers, D. 1975, Circumstellar envelopes and mass loss of red giant stars (Problems in stellar atmospheres and envelopes.), 229
Remus, F., Mathis, S., & Zahn, J.-P. 2012, A&A, 544, A132
Rieutord, M. 2006, A&A, 451, 1025
Rogers, T. M., & Glatzmaier, G. A. 2005, MNRAS, 364, 1135
Rogers, T. M., & Glatzmaier, G. A. 2006, ApJ, 653, 756
Rogers, T. M., MacGregor, K. B., & Glatzmaier, G. A. 2008, MNRAS, 387, 616
Rudiger, G., & Kitchatinov, L. L. 1997, Astron. Nachr., 318, 273
Samadi, R., Belkacem, K., Goupil, M. J., et al. 2010, Ap&SS, 328, 253
Schatzman, E. 1993, A&A, 279, 431
Spada, F., Lanzafame, A. C., & Lanza, A. F. 2010, MNRAS, 404, 641
Spruit, H. C. 1999, A&A, 349, 189
Strugarek, A., Brun, A. S., & Zahn, J.-P. 2011, A&A, 532, A34
Suijs, M. P. L., Langer, N., Poelarends, A.-J., et al. 2008, A&A, 481, L87
Talon, S., & Charbonnel, C. 1998, A&A, 335, 959
Talon, S., & Charbonnel, C. 2003, A&A, 405, 1025
Talon, S., & Charbonnel, C. 2004, A&A, 418, 1051
Talon, S., & Charbonnel, C. 2005, A&A, 440, 981
Talon, S., & Charbonnel, C. 2007, in Why Galaxies Care About AGB Stars: Their Importance as Actors and Probes, eds. F. Kerschbaum, C. Charbonnel, & R. F. Wing, ASP Conf. Ser., 378, 137
Talon, S., & Charbonnel, C. 2008, A&A, 482, 597
Talon, S., & Zahn, J.-P. 1997, A&A, 317, 749
Talon, S., Zahn, J.-P., Maeder, A., & Meynet, G. 1997, A&A, 322, 209
Talon, S., Kumar, P., & Zahn, J.-P. 2002, ApJ, 574, L175
Turck-Chièze, S., Palacios, A., Marques, J. P., & Nghiem, P. A. P. 2010, ApJ, 715, 1539
Ud-Doula, A., Owocki, S. P., & Townsend, R. H. D. 2009, MNRAS, 392, 1022
Zahn, J.-P. 1977, A&A, 57, 383
Zahn, J.-P. 1983, in Saas-Fee Advanced Course 13: Astrophysical Processes in Upper Main Sequence Stars, eds. A. N. Cox, S. Vauclair, & J. P. Zahn, 253
Zahn, J.-P. 1992, A&A, 265, 115
Zahn, J.-P., Talon, S., & Matias, J. 1997, A&A, 322, 320
Zahn, J.-P., Brun, A. S., & Mathis, S. 2007, A&A, 474, 145